frontiers in Materials

ORIGINAL RESEARCH
published: 10 February 2022
doi: 10.3389/fmats.2022.833065

Enhanced Mechanical Properties of 3D Printed Nanocomposites Composed of Functionalized Plant-Derived Biopolymers and Calcium-Deficient Hydroxyapatite Nanoparticles

*Dibakar Mondal, Elizabeth Diederichs and Thomas L. Willett**

Composite Biomaterial Systems Laboratory, University of Waterloo, Waterloo, ON, Canada

OPEN ACCESS

Edited by:
R. A. Ilyas, University of Technology Malaysia, Malaysia

Reviewed by:
Antonio Greco, University of Salento, Italy
Junheng Zhang, South-Central University for Nationalities, China

***Correspondence:**
Thomas L. Willett
thomas.willett@uwaterloo.ca

Specialty section:
This article was submitted to Polymeric and Composite Materials, a section of the journal Frontiers in Materials

Received: *10 December 2021*
Accepted: *19 January 2022*
Published: *10 February 2022*

Citation:
Mondal D, Diederichs E and Willett TL (2022) Enhanced Mechanical Properties of 3D Printed Nanocomposites Composed of Functionalized Plant-Derived Biopolymers and Calcium-Deficient Hydroxyapatite Nanoparticles. Front. Mater. 9:833065. doi: 10.3389/fmats.2022.833065

The combination of plant-derived polymer resins and mineral-based nanoparticles into three dimensional (3D) printable, high-performance nanocomposites suggests a means to improve the sustainability profile of rapid prototyping and additive manufacturing. In this work, our previously published nanocomposite biomaterial system of acrylated epoxidized soybean oil (AESO) and polyethylene glycol (PEGDA) diluent composited with calcium-deficient hydroxyapatite (nHA) nanorods was improved by the substitution of AESO with methacrylated AESO (mAESO) and the partial substitution of PEGDA with isosorbide methacrylate (IM). mAESO was used to increase the degree of crosslinking and reduce the ink viscosity. IM was synthesized by reacting the hydroxyl groups on isosorbide with methacrylic anhydride. The effects of partially replacing PEGDA with IM on the rheology and printability of the nanocomposite inks and the mechanical properties of the resulting nanocomposite materials were quantified. These masked stereolithography (mSLA) printed nanocomposites have greatly improved mechanical properties (tensile strength, Young's modulus, and Mode-I fracture toughness) due to the shift to mAESO and IM. IM greatly improved the tensile fracture strength and Young's modulus of the nanocomposites by acting as a reactive diluent and as a stiff segment in the polymer system. Dynamic mechanical analysis revealed that the glass transition temperature of the nanocomposite increased due to the addition of IM. However, IM decreased the strain-at–fracture, making the nanocomposites more brittle. This study demonstrates the development of high-performance mAESO-IM-nHA-based novel nanocomposites that can be easily 3D printed using desktop mSLA, suggesting a facile path forward to improved sustainability in rapid prototyping and additive manufacturing using nanocomposites for a broad range of applications.

Keywords: 3D printing, polymer nancomposite, biopolymer, acrylated epoxidized soybean oil (AESO), isosorbide methacrylate, hydroxyapatite

INTRODUCTION

The majority of commercially available UV-curing thermoset polymers are of petrochemical origin. Their production is not conducive to the critical need to reduce harmful carbon emissions (Babu et al., 2013; Amulya et al., 2021). Plant-derived or vegetable oil-based polymers may lower or even capture carbon emissions (Bertomeu et al., 2012; Llevot, 2017; Amulya et al., 2021) because their production results partially from photosynthesis. As biopolymeric materials, they are advantageous over petroleum-based polymers or animal-derived natural polymers due to their versatility, renewability, and biodegradability (Bertomeu et al., 2012; Llevot, 2017; Saxon et al., 2020; Amulya et al., 2021). Acrylated epoxidized soybean oil (AESO) is a vegetable oil-derived acrylate monomer. It is synthesized by adding epoxides to the unsaturated parts of the triglyceride chains of soybean oil and then replacing these epoxides with acrylate groups (Pelletier and Gandini, 2006; Song et al., 2006; Mauck et al., 2016). Renewable, eco-friendly, biodegradable, and multifunctional thermoset polymer artifacts can be produced by light-assisted free radical polymerization of AESO (La Scala and Wool, 2005; Campanella et al., 2009; Campanella et al., 2011). However, due to the low count of unsaturated bonds in each triglyceride chain of AESO, the yield of acrylate functionalization is low. An average of two to three hydroxyl (-OH) groups per molecule are functionalized with acrylate groups and two to three residual -OH groups remain. These hydroxyls increase the viscosity of the AESO based resin through hydrogen bonding, and the low acrylate group count limits the strength of the polymerized AESO. To lower the viscosity for easier processing and printing, and to increase the strength through an increased degree of crosslinking, it would be beneficial to replace these residual -OH groups with acrylate/methacrylate groups that can be polymerized through similar processes (Liu et al., 2017). One such product is known as methacrylated AESO (mAESO).

It is important to improve the mechanical performance of sustainable biomaterials to compete with commonly used petroleum-based polymers and polymer nanocomposites (Zhu et al., 2016; Schneiderman and Hillmyer, 2017). Isosorbide is an excellent candidate as an additive to achieve such mechanical properties. It is a monomer derived from glucose, which is abundantly available from cellulose and starch (Wang et al., 2016). Isosorbide can act as a building block to create high-performance biopolymer-based materials (Fenouillot et al., 2010; Galbis et al., 2016). Isosorbide-based copolymers are attracting interest as sustainable polymers to replace traditional petro-based polymers to apply in the fields of automobiles, biomedical applications, coatings, pressure-sensitive adhesives, and nanofibers (Saxon et al., 2020). Isosorbide has two cis-fused tetrahydrofuran rings and secondary alcohols at the 2- and 5-positions. It is quite stiff due to its ring structure and therefore can act as a stiff segment in co-polymerization schemes. The -OH groups have relatively low reactivity. This poses a major challenge to step-growth polymerization to produce longer chains (M_n > 10 kDa) and higher isosorbide content (>50 mol%) (Fenouillot et al., 2010). High temperature, prolonged reaction time, and complex reaction processes are required to prepare long-chain isosorbide polymers (Fenouillot et al., 2010). In addition, co-polymerization of isosorbide with another polymer often requires the use of toxic reagents, such as phosgene, isocyanates, etc., which challenges their sustainability (Saxon et al., 2020). These issues can be overcome by adding suitable functional groups (such as methacrylate/acrylate groups) to isosorbide before polymerization or copolymerization (Liu et al., 2017) to prepare functional isosorbide (such as isosorbide methacrylate, IM). Thermosets of IM have a glass transition temperature greater than 240°C and thermally decompose at over 400°C (Sadler et al., 2013). The flexural strength and modulus are 85 MPa and 4 GPa, respectively, making it a high-performance thermoset better than any known vinyl ester resin and comparable to expensive high-temperature epoxy resins (Sadler et al., 2013). Polymers made of blending IM and mAESO have higher flexural strength, flexural modulus, flexural strain, storage modulus, glass transition temperature, and thermal stability compared to IM and AESO-based thermosets (Liu et al., 2017). To the best of the authors' knowledge, and despite the excellent mechanical and biodegradation properties of isosorbide-based polymers, there are no reports on nanocomposites made of ceramic or mineral nanoparticles and isosorbide or its derivatives.

Masked stereolithography (mSLA) is a high-resolution additive manufacturing process where light-sensitive liquid resin is solidified (cured) *via* selective exposure to light [commonly ultraviolet (UV)] in a layer-by-layer process. Compared to other three-dimensional (3D) printing techniques, such as fused deposition modeling (FDM), direct ink writing (DIW), or stereolithography (SLA), mSLA printing methods are inexpensive and provide solid prints with minimal defects (Mondal et al., 2021; Muenks and Kyosev, 2021; Podgórski et al., 2021). It is a relatively fast printing technology as it prints each layer all at once by light/UV masking using an LCD screen, rather than point-by-point extrusion or curing (Mondal et al., 2021; Muenks and Kyosev, 2021; Podgórski et al., 2021). However, the selection and development of materials as inks for mSLA-based 3D printing is a technical challenge. The rheological properties of the ink must be suitable to allow for the print-bed to move within the resin reservoir (Ligon et al., 2017; Podgórski et al., 2021). Among the vast library of biopolymers, the choice of biopolymers for mSLA-based 3D printing is limited due to their rheological properties, their potential for photo-polymerization, and the resulting mechanical properties. A solution to this problem is the chemical modification of suitable bioderived monomers (such as soybean oil and isosorbide) by the addition of functional groups that can undergo photopolymerization.

In this work, hydroxyapatite (HA) nanoparticles were composited with an IM-mAESO resin matrix to fabricate biopolymer nanocomposites using mSLA for the first time. The effects of IM content on the tensile and fracture mechanical properties of mAESO-based 3D printed nanocomposites were studied. HA nanoparticles are relatively facile to produce and have physical and chemical properties resembling those of natural bone mineral (de Bruijn et al.,

1992; Webster et al., 2000; Rosa et al., 2002). We hypothesized that the addition of IM would decrease the viscosity of the nanocomposite ink and improve the dispersion of the nanoparticles within the cured nanocomposite. Additionally, it was hypothesized that IM would increase the ultimate tensile strength and fracture toughness of the nanocomposites by working as a stiff segment in between the more flexible triglyceride chains.

MATERIALS AND METHODS

Materials

Acrylated epoxidized soybean oil (AESO; average molecular weight (MW) of 1200), polyethylene glycol diacrylate (PEGDA; MW of 250), methacrylic anhydride (MAA), phenylbis (2,4,6-trimethylbenzoyl) phosphine oxide (Irgacure 819), and sodium hydroxide (NaOH) were purchased from Sigma Aldrich Co. D-Isosorbide and 4-(dimethyl amino)pyridine (DMAP) were purchased from Alfa Aesar Co. Nanohydroxyapatite powder (nHA) (~120 nm long and 30–40 nm diameter rod-shaped) was purchased from MKnano Inc. (Mississauga, Canada). This calcium-deficient nHA has an average Ca/P of 1.52, a specific gravity of 2.92, and a crystallinity index of 0.52–0.54 (Comeau and Willett, 2018).

Synthesis of Isosorbide Methacrylate (IM) and Methacrylate Functionalized AESO (mAESO)

IM and mAESO were prepared by following the methods of Liu et. al (Liu et al., 2017), except in this work, the IM and mAESO were synthesized separately. To synthesize IM, 29.4 g of D-isosorbide (0.2 mol) and 1.22 g DMAP (0.01 mol) were added to 89.4 ml MAA (0.6 mol) in a glass beaker. The mixture was placed in a water bath at 60°C with gentle stirring (300 rpm) for 6 h. After 6 h, the mixture was removed from the water bath and allowed to cool to room temperature. The synthesized IM was separated and purified by reacting the mixture with 100 ml of 0.5 M NaOH solution for 10 min. After 10 min, the mixture stood for an hour to allow the IM to settle at the bottom. The clear solution from the top was aspirated off. The purification of IM using 0.5 M NaOH solution was repeated one time. Next, the reaction product was mixed with 100 ml deionized water for 10 min and then stood for an hour. The purified IM settled at to bottom of the beaker. After aspiring off the top clear solution, purification with water was also repeated one time. Finally, the purified IM was dried in a desiccator chamber under reduced pressure.

To synthesize mAESO, 0.51 g of DMAP (0.004 mol) was added to 39.7 ml of MAA (0.25 mol) and dissolved by stirring at 500 rpm. Then 50 g of AESO (AESO:MAA molar ratio of 1:6) was added to the MAA and DMAP mixture and placed in a water bath at 60°C with continuous stirring at 500 rpm. After 24 h, the reaction products were washed sequentially with 100 ml of 0.5 M NaOH solution and deionized water. After each wash, pale-yellow mAESO settled to the bottom of the glass beaker. Finally, it was dried in a desiccator chamber under reduced pressure.

Preparation of Nanocomposite Inks

The required amounts of mAESO and PEGDA were weighed and mixed in a polypropylene beaker. Then, the Irgacure 819 photoinitiator was dissolved into this resin mixture at 1% of total ink volume using an ultrasonic homogenizer (Branson Sonifier 450, Emerson Inc., United States) for 5 min nHA powder was then added to the mixture at 10 vol% and dispersed using the ultrasonic homogenizer for another 5 min. The nHA powder was further homogenized by using a mechanical homogenizer (Unidrive X 1000, M. Zipperer GmbH, Germany) for 2 min. Dispersion of nHA powder in the resin matrix was repeated twice using both homogenizers. Next, the IM was added to the ink mixture and mixed by hand. The volumetric percentage of mAESO to total resin was kept constant to 50 vol%. The ratios of IM:PEGDA were varied for different nanocomposites. Four inks were prepared, and their compositions are summarized in **Table 1**. The composition of an AESO/PEGDA/nHA-based nanocomposite ink (SP10) reported earlier (Mondal et al., 2021) has been added to this table for comparison.

Rheology, Cure Depth, and Thermogravimetric Analysis of the Nanocomposite Inks

The rheological properties (viscosity and shear yield strength) and cure depth curve of the inks, and the composition and thermal degradation of the nanocomposite inks [assessed using thermogravimetric analysis (TGA)] were measured in accordance with protocols previously used by our research group (Mondal et al., 2021).

mSLA-Based 3D Printing

mSLA-based 3D printing was performed using a Phrozen Sonic XL 4 K (Phrozen Technology, Taiwan). Initially, 3D stereolithographic (.stl) files were sliced using the Phrozen slicer software. All specimens were printed with a layer height of 50 μm. Each layer was exposed to UV for 6 s, except for the first six layers, which were cured for 15 s to ensure good build plate adhesion. After completion of 3D printing, the specimens were carefully removed from the print bed using a metal spatula and wiped thoroughly. To avoid uncured ink residue on the surfaces of the specimens, they were exposed to additional UV in a post-print curing chamber (CureZone MKII, Creative CADWORKS, Canada) for 10 min on each side, and then thoroughly rinsed with ethanol for approximately 5 min.

Dispersion of Nanoparticles

Dispersion of the nanoparticles within the cured resin matrices was observed using scanning electron microscopy (SEM). 3D printed specimens were polished sequentially by using 6, 1, and

TABLE 1 | Nomenclature and composition of the nanocomposites.

Nomenclature	AESO (vol%)	mAESO (vol%)	PEGDA (vol%)	IM (vol%)	nHA (vol%)
SP10	45	—	45	—	10
IM0	—	45	45	0	10
IM10	—	45	36	9	10
IM20	—	45	27	18	10
IM30	—	45	18	27	10

0.5 μm diamond suspensions before mounting on SEM tabs. The specimens were gold-coated for 120 s. SEM was conducted using a LEO FE-SEM 1530 (ThermoFisher Scientific, United States), using both Secondary Electron (SE) and Back-Scattered Electron (BSE) modes.

Print Fidelity

The print fidelity of each nanocomposite ink was evaluated by measuring various 3D printed rectangular and cylindrical specimens and comparing their cross-sectional areas (CSA) with the design. The printability was calculated as:

$$Printability, \Pr = \frac{CSA\ of\ 3D\ printed\ object}{CSA\ of\ designed\ object}$$

If the print fidelity was perfect, Pr would be equal to 1.

Tensile Mechanical Properties

Dogbone-shaped test specimens [overall length = 30 mm, gauge length = 10 mm, gauge length width = 2.5 mm, and thickness = 2 mm; based on ASTM D3039 (ASTMD3039, 2017)] were printed using the mSLA 3D printer. The Phrozen Slicer software was used to set the orientation and for the addition of necessary supports. Support material consisting of six support fixtures per specimen was added in the grip areas to avoid defects and damage to the gauge length of the specimens during printing and removal from the print bed.

Tensile testing was performed using a Psylotech μTS mechanical testing machine (Psylotech Inc., Evanston, IL, United States) with a 1.6 kN windowing load cell. Strain measurement was conducted using microscope-enabled digital image correlation (DIC; Vic 2D 6, Correlated Solutions Inc., United States). A microscope (BXFM, Olympus Corp., Center Valley, PA, United States) with a digital camera (Point Grey, 5 MP, 2/3" detector) was mounted over the test system to take magnified images of the gauge length during the test. A ×2.5 magnification objective lens (Olympus Corp., Center Valley, PA, United States) was used. The resulting spatial resolution was 1450 pixels mm^{-1}.

The specimens (n = 7 per group) were sprayed with high-resolution toner powder (Xerox Phaser 6000) using an atomizer jar to create speckle patterns, enabling DIC strain measurement. These particles were 4–5 μm in diameter. In displacement control mode, specimens were first preconditioned at 1 Hz for 100 cycles. Then extension was applied at a rate of 16 μm/s speed (average strain rate of 0.0016 s^{-1}). All testing was carried out at room temperature. Data were acquired at 5 Hz. The average engineering strains were measured from the DIC using a line extensometer tool. The engineering stress was calculated by dividing the applied load by the initial cross-sectional area. True strain (ε_t) was also calculated, using the formula,

$$\varepsilon_t = \ln\left(\frac{l}{l_0}\right)$$

Both the current length (l) and original length (l_0) were obtained from the extensometer tool. The transverse strain (y-axis) was calculated using the extensometer tool. It was assumed the z-axis strain would be the same as the transverse strain; therefore, it was possible to calculate the true cross-sectional area for each data point. Therefore, the true stress was calculated by dividing the applied load by the true cross-sectional area. Young's modulus was determined from the slope of the initial linear elastic portion (0–0.3% strain) of the stress-strain curve. Yield strength was calculated using a conventional 0.2% offset from the linear portion of the curve. Toughness values were obtained as the area under the stress-strain curves up to the point of fracture. Poisson's ratio (ν) was calculated by following the ASTM standard for tensile testing, and using the formula:

$$\nu = -\frac{\Delta\varepsilon_t}{\Delta\varepsilon_l}$$

where ν is taken as the slope of the ε_t -ε_l plot.

Fracture Toughness Testing

Single-point fracture toughness (K_{1c}) of each of the mSLA-printed nanocomposites was measured using the same testing frame but equipped with a 3-point bending fixture and performed according to ASTM D5045-14 (ASTM, 2016). Single edge notch bending (SENB) test specimens with the length of 50 mm (gauge length 40 mm), thickness (B) of 5 mm, and a width (W) of 10 mm were 3D printed, with the same method as the specimens for tensile testing (Section *mSLA-Based 3D Printing*). A 4.5 mm notch was cut into the width using an IsoMet^{tm} low-speed metallurgical saw (Buehler Ltd., IL, United States) and a starter crack was created by tapping the specimens gently with a sharp razor blade placed in the notch. The initial crack lengths (a_0) fell within the $0.45 < a/W < 0.55$ specification. All testing (n = 6) was conducted at room temperature and in displacement control mode with a crosshead speed of 3.3 μm/s. Data were acquired at 5 Hz. Plane strain fracture toughness was calculated by the standard equation,

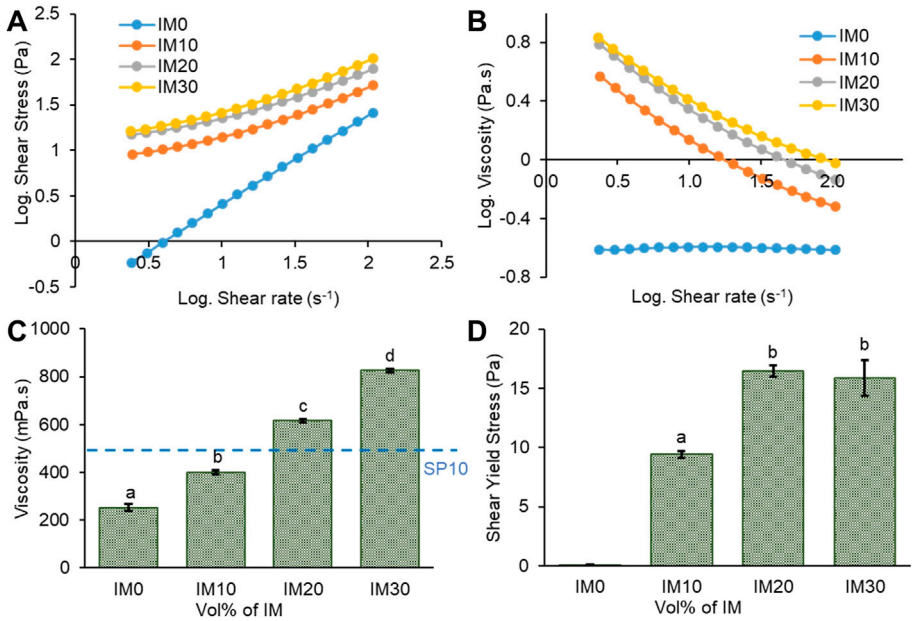

FIGURE 1 | Rheological behavior of the nanocomposite inks. **(A,B)** Representative log-log plots of shear stress and viscosity vs shear rate. **(C)** Viscosities and **(D)** yield shear strengths of the nanocomposite inks. The viscosity and yield shear strength values were calculated from the slopes and the *y*-axis intercepts, respectively, of the shear stress vs shear rate plots. The dotted blue line in panel **(C)** represents the viscosity value of SP10 (Mondal et al., 2021). Data are presented as mean ± SD ($n = 3$ of each composition). One-way ANOVA and Tukey's multiple comparison test were used for statistical analysis. Different small-case letters indicate statistical significance at $p < 0.05$.

$$K_Q = \left(\frac{P_Q}{BW^{0.5}}\right)\left[6\,(\mathrm{a/w})^{0.5}\frac{\left[1.99-\frac{a}{W}\left(1-\frac{a}{W}\right)\left(2.15-3.93\frac{a}{W}+2.7\frac{a^2}{W^2}\right)\right]}{\left(1+2\frac{a}{W}\right)\left(1-\frac{a}{W}\right)^{1.5}}\right]$$

K_Q was considered as K_{1c} if

$$2.5\left(\frac{K_Q}{\sigma_y}\right)^2 < B, a, and\,(W-a)$$

Where a is the initial crack length, P_Q is the load, and B and W are the thickness and width of the specimen, respectively.

Dynamic Mechanical Analysis and Glass Transition Temperature

DMA was conducted using a Q800 dynamic mechanical analyzer (TA Instruments, New Castle, Delaware, United States) in three-point bending mode with dual cantilever clamps. Test specimens with a length of 120 mm, a width of 12 mm, and a thickness of 3 mm were 3D printed as in *Section mSLA-Based 3D Printing*. Specimens were scanned at the frequency of 1 Hz from 25 to 150°C at a heating rate of 3°C/min using a liquid nitrogen cooling accessory. For SP10 and IM0, the tests were stopped at 95 and 120°C, respectively, as the storage moduli plateaued.

Statistical Analyses

Data are presented as mean ± standard deviation (SD). All data were analyzed using SigmaStat (Version 4.0, Systat Software Inc., CA, United States). Means were compared using one-way analysis of variance (ANOVA) followed by Tukey's multiple comparison test. Differences between means were considered statistically significant at $p < 0.05$.

RESULTS

Rheology, Cure Depth, and Printability of the Nanocomposite Inks

The rheological performance of the four nanocomposite inks is reported in **Figure 1**. The ink without IM (IM0) demonstrated Newtonian behavior with zero shear yield stress (**Figure 1A**). IM-containing nanocomposite inks demonstrated shear yield strength as the shear rate was reduced to zero (**Figure 1B**). Viscosity values decreased as the shear rates increased, showing distinct shear-thinning behavior of these IM-containing nanocomposites. Consistent viscosity values appeared for shear rates exceeding 40 s^{-1}. The viscosity and shear yield strength values were calculated from the slopes and the *y*-axis intercept values of the shear stress vs shear rate curves and plotted in **Figures 1C,D**. Replacing AESO with mAESO decreased the viscosity from 490 mPa s (SP10) (Mondal et al., 2021) to 253 mPa s (IM0). The ink viscosities increased with increasing IM content. The addition of 27 vol% IM (IM30) increased the viscosity from 253 ± 15 mPa s (IM0) to 826 ± 6 mPa s (227% increase). IM content also introduced shear yield strength to the nanocomposite inks. IM10 and IM20 inks had 9.4 ± 0.3 Pa and 16.5 ± 0.5 Pa shear yield strength, respectively (**Figure 1D**). The shear yield strengths of IM20 and IM30 were not statistically different.

The layer height and the duration for 3D printing of each layer were determined by plotting the standard cure depth curve for each nanocomposite (**Figure 2A**). These plots are the best fit curve of cured depths in response to various UV doses for the nanocomposite inks. Variation of IM content did not affect the

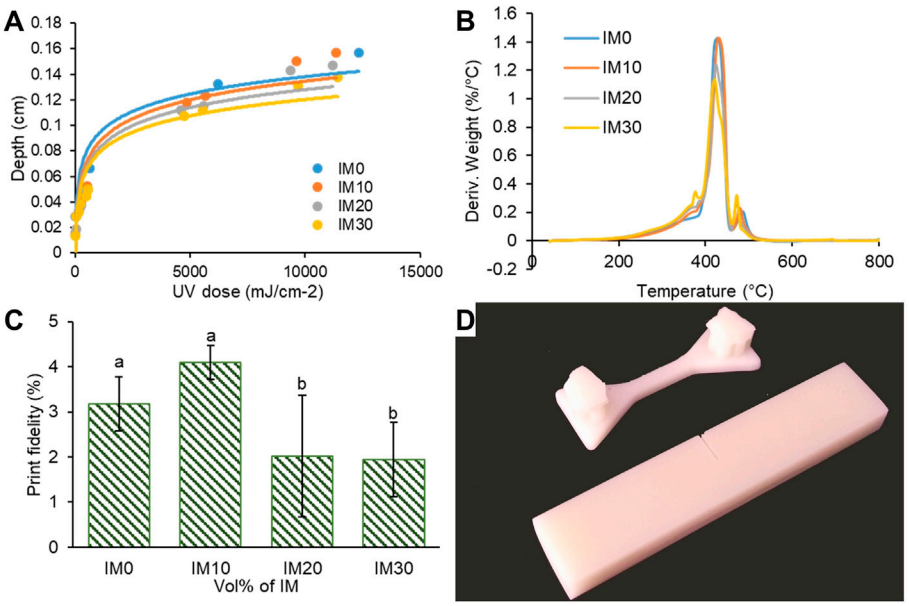

FIGURE 2 | (A) Cure depth vs UV energy dosage for mAESO/IM/PEGDA/nHA nanocomposite inks. **(B)** Representative derivative weight loss thermograms of cured nanocomposites. **(C)** Print fidelity of the nanocomposites calculated by measuring the percent error of 3D printed objects. Data are presented as mean ± SD ($n = 7$ of each composition). One-way ANOVA and Tukey's multiple comparison test were used for statistical analysis. Different small-case letters indicate statistical significance at $p < 0.05$. **(D)** 3D printed dogbone-shaped tensile test specimens and rectangular beams for SENB fracture test specimens using the IM20 nanocomposite ink.

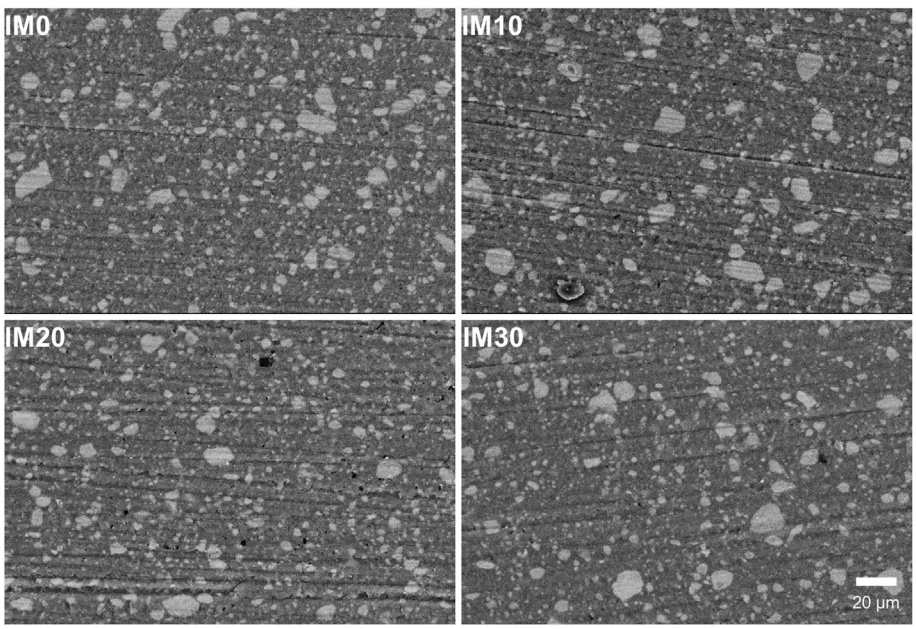

FIGURE 3 | Representative backscattered mode SEM images of the different nanocomposites. Brighter spots indicate micron-sized agglomerates of nHA particles. Dispersion and agglomerate size and shape were consistent between the groups.

cure depth. Thermogravimetric analysis (TGA) was conducted to evaluate the inorganic nHA content in the nanocomposite inks. The derivative mass loss curve against temperature in **Figure 2B** shows that all the nanocomposites burned in the range of 300–500°C in a similar fashion. The residual mass presumably corresponds to the inorganic nHA particles. The weight and volume percentage of nHA to the nanocomposites are listed in **Supplementary Table S1** The Print fidelity of the

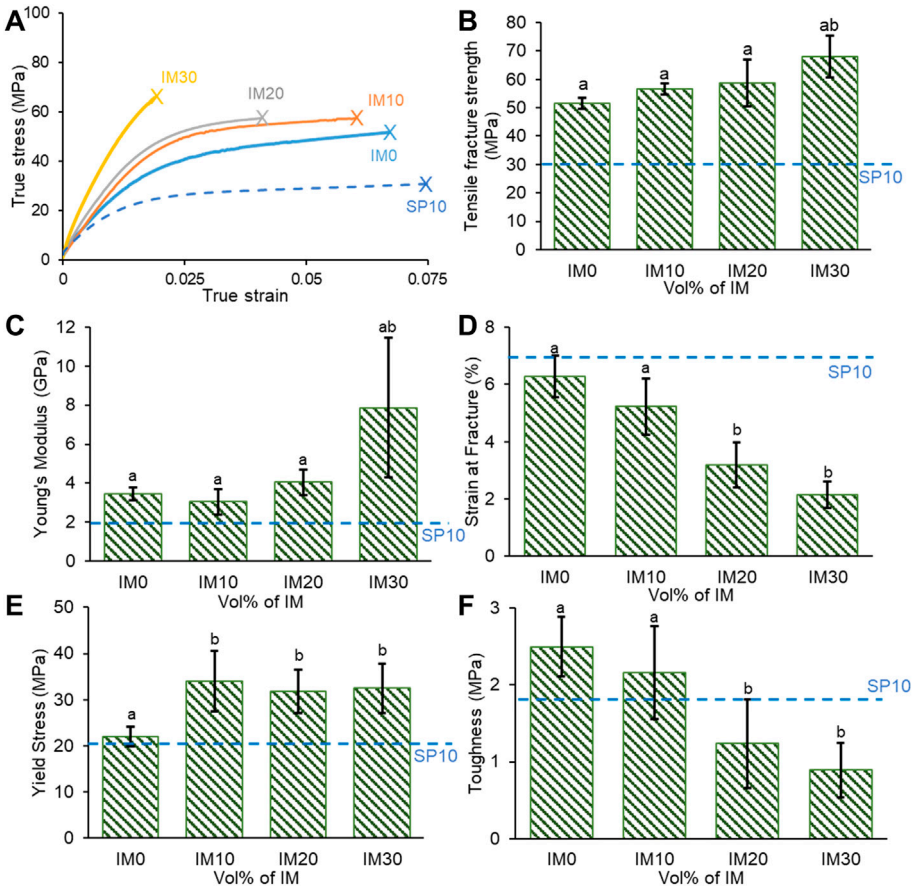

FIGURE 4 | Tensile mechanical properties of the mSLA-printed nanocomposites: **(A)** representative true stress vs true strain curves, **(B)** tensile fracture strengths (ultimate tensile strengths), **(C)** Young's moduli, **(D)** strains-at-fracture, **(E)** yield strength, and **(F)** toughness. For panels **(B–F)**, data are presented as mean ± SD ($n = 7$ specimens of each composition). One-way ANOVA and Tukey's multiple comparison test were used for statistical analysis. Different small-case letters indicate statistical significance at $p < 0.05$. The dotted blue line represents the corresponding values of SP10, an AESO/PEGDA/nHA based nanocomposite from our previous work (Mondal et al., 2021).

nanocomposites calculated by measuring the percent error of 3D printed objects (**Figure 2C**). Panel D **Figure 2D** represents a human vertebra 3D printed by using IM20 nanocomposite inks, showing the excellent printability of the nanocomposites.

Dispersion of Nanoparticles in Biopolymer Matrices

SEM images of polished and gold-coated surfaces of the 3D printed nanocomposites are shown in **Figure 3**. The size (2–10 μm) and shape of the HA particle agglomerates were consistent regardless of the resin compositions.

Tensile Mechanical Properties of the 3D Printed Nanocomposites

Representative true stress versus strain curves and plots of the measured tensile fracture strength (ultimate tensile strength), Young's modulus, strain-at-fracture, yield strengths, and toughnesses are provided in **Figure 4**. IM containing nanocomposites had higher tensile fracture strengths than IM0 (**Figures 4A,B**). IM30 tensile strength and modulus values were 65.99 ± 8.78 MPa and 7.46 ± 3.50 GPa, respectively. This equated to a 28 and 115% increase in properties from IM0, respectively. The incorporation of IM into the mAESO/PEGDA resin improved the tensile fracture strength and modulus significantly and decreased the fracture strain. IM30 nanocomposites fractured at 2.07 ± 0.49% elongation, which is a 67% decrease from IM0 (6.27 ± 0.73%).

The incorporation of IM significantly improved the yield strength of the nanocomposites (**Figure 4E**). However, variation of IM did not have a significant impact on yield strength. The toughness of the nanocomposites drastically decreased with increased IM content (**Figure 4F**). The average toughness of the IM30 (0.89 ± 0.36 MPa) was 64% lower than IM0 (2.50 ± 0.40 MPa). The changes in Poisson's ratios amongst the nanocomposites were small and not statistically significant (**Supplementary Figure S2**). The dotted blue line represents the corresponding values of SP10, an AESO/PEGDA/nHA based nanocomposite from our previous work (Mondal et al., 2021),

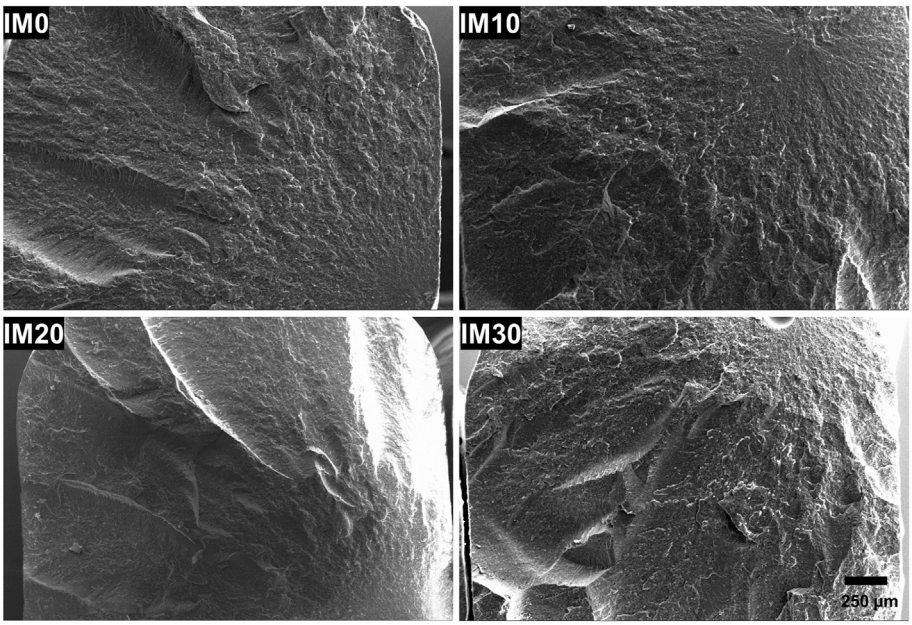

FIGURE 5 | SEM images of the fracture surfaces after tensile testing.

analogous to IM0. Compared with the tensile mechanical properties of SP10, the fracture strength and modulus dramatically increased by replacing AESO with mAESO. However, similar to the incorporation of IM, mAESO made the nanocomposites more brittle, evident by the lower strain-at-fracture values.

The tensile fracture surfaces were imaged using SEM (**Figure 5**). The absence of defects and entrapped bubbles indicate excellent processing and printing of these nanocomposites. All the nanocomposites showed brittle fracture behavior through micro-scale roughness with "rive-pattern" fracture surfaces which include lines and ridges. The apparent absence of macro or micro-scale plastic deformation zones indicates brittle fracture.

Plain Strain Fracture Toughness of the 3D Printed Nanocomposites

Representative load versus load-line deflection curves from the fracture toughness tests are plotted in **Figure 6A**. All the nanocomposites demonstrated brittle fracture with fast unstable crack growth at peak load. The Mode-I plane strain fracture toughness values (K_{IC}) for the nanocomposites are plotted in **Figure 6B**. These results were verified to be valid K_{IC} values in accordance with the ASTM D5045 standard. The incorporation of IM did not significantly change the fracture toughness of the nanocomposites, but replacing the AESO with mAESO did improve the fracture toughness.

Fracture surfaces from SENB specimens after testing are consistent with the fracture surfaces from the tensile test specimens (**Figure 7**). The crack propagation directions are indicated by the white arrows. The fracture surfaces of the nanocomposites are smooth and essentially featureless, which indicates a typical brittle characteristic for highly crosslinked polymeric resins.

Dynamic Mechanical Analysis of the 3D Printed Nanocomposites

DMA was performed to study the viscoelastic behavior and measure the glass transition temperatures of the 3D printed nanocomposites. The storage modulus (E′), loss modulus (E″), and damping coefficient (tanδ) of each specimen were measured. The E′ and tanδ as a function of temperature are plotted in **Figure 8**. The replacement of AESO with mAESO greatly improved the dynamic mechanical behavior of the nanocomposites. At room temperature, the storage modulus of IM0 increased to double compared to that of SP10 (**Figure 8A**). Incorporation of IM increased the E′ of the nanocomposites, consistent with the tensile testing results. IM30 had the highest storage modulus at any given temperature. **Figure 8B** represents the tanδ curves from which the T_g of the nanocomposites were determined from the respective peaks. Replacing AESO with mAESO increased the T_g from 64°C (SP10) to 89°C (IM0). The incorporation of IM dramatically increased the T_g of the nanocomposites as well. The T_g of IM0 was 89°C and increased to 142°C in the IM30 nanocomposite.

DISCUSSION

We have demonstrated the mSLA-based 3D printability of AESO/PEGDA/nHA nanocomposites in our previous work (Mondal et al., 2021). Due to the high viscosity of AESO, a

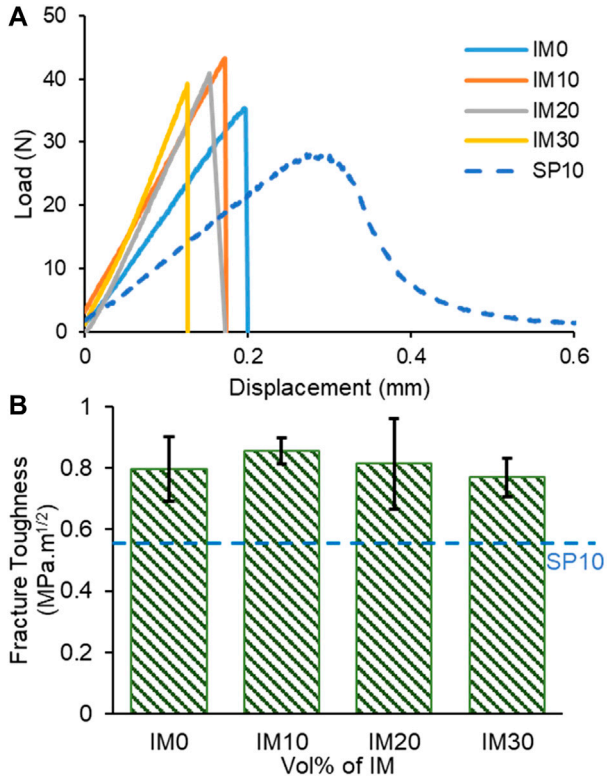

FIGURE 6 | Fracture behavior of the nanocomposites: **(A)** representative load versus load-line deflection curves from SENB tests, and **(B)** corresponding plane-strain fracture toughness (K_{1C}) values. Data are presented as mean ± SD (n = 7). One-way ANOVA and Tukey's multiple comparison test were used for statistical analysis. Data are not statistically different. The dotted blue line represents the corresponding values for SP10, an AESO/PEGDA/nHA based nanocomposite from our previous work (Mondal et al., 2021).

significant volume fraction of the resin (50%) was the reactive diluent, PEGDA, which was required to improve the printability by achieving a printable viscosity and improved dispersion of nHA into the nanocomposite inks. Although PEGDA is a petroleum-based polymer, it was beneficial as it improved the mechanical properties of the 3D printed nanocomposites (Mondal and Willett, 2020; Mondal et al., 2021). To develop more sustainable biopolymer nanocomposites, we examined the development of nHA-containing nanocomposites using lower viscosity and bio-based mAESO and IM, allowing for both a lower volume fraction of PEGDA and greater mechanical performance.

In this work, mAESO, PEGDA, and IM were composited with calcium-deficient hydroxyapatite nanoparticles to prepare sustainable 3D printable nanocomposites. The PEGDA was partially replaced with IM and the effects on rheological, tensile, and fracture properties were studied. The rheological data did not support the hypothesis that the addition of IM would decrease the viscosity of the nanocomposite inks and improve the dispersion of nanoparticles. The viscosity increased with increasing IM content and had no detectable effect on the nHA dispersions, and yet the inks were still printable as tensile and fracture test specimens.

Liu et al. reported that mAESO has a lower viscosity than AESO due to the lack of –OH groups and related hydrogen bonding (Liu et al., 2017). Additionally, IM (12 mPa.s) reportedly has a lower viscosity value than PEGDA (13.4–20 mPa s) (Moon et al., 2015; Liu et al., 2017; Han et al., 2019). Theoretically, with the use of mAESO and the replacement of PEGDA with IM, the viscosity of the nanocomposite ink should have decreased according to the basic Rule of Mixtures, leading to improved printability. Replacing AESO with mAESO decreased the viscosity of the nanocomposite inks by half, when comparing between IM0 (mAESO:PEGDA is 50:50) and SP10 (AESO:PEGDA is 50:50) nanocomposite inks (Mondal et al., 2021). However, the lowering of ink viscosity by mAESO was suppressed by replacing PEGDA with IM. Moreover, the addition of IM introduced shear yield strength to the nanocomposite inks, which is presumably due to the result of hydrogen bonding between the calcium-deficient nHA and the IM. This hydrogen bonding might form between the O groups from the difuran structure of IM and the –OH on the nHA. In mSLA-based 3D printing, inks with low viscosity and negligible shear yield strength are required so that the build platform can move freely during printing, and the ink can quickly refill the gap between the printed object and the bottom of the ink reservoir. 5000 mPa s is the recommended upper limit viscosity for ceramic nanoparticle-containing nanocomposite inks for mSLA-based 3D printing (Stansbury and Idacavage, 2016; Gonzalez et al., 2017; Ligon et al., 2017; Mu et al., 2017). The viscosity of our nanocomposite inks is below this threshold. Moreover, the absence of defects or bubbles in the SEM images of the 3D printed testing specimens indicates the shear yield strengths of the nanocomposite inks are too low to alter the printability and introduce other strength limiting defects within the microstructure of the 3D printed nanocomposites.

Although the strain-at-fracture decreased, the tensile fracture strength and modulus were drastically increased by replacing AESO with mAESO; comparing current nanocomposites with our previously reported nanocomposite SP10 (Mondal et al., 2021). Replacing PEGDA with IM similarly increased the tensile fracture strength and Young's modulus, while also decreasing the strain-at-fracture, in a dose-dependent manner. IM30 was 28% stronger and 115% stiffer than the IM0 nanocomposite. These increases are the result of the higher degree of crosslinking due to the mAESO, and inclusion of the shorter chain and cyclic structure of IM, which acts as a stiff segment within the resin, greatly affecting the chain mobility and increasing the glass transition temperature (Fenouillot et al., 2010; Wilbon et al., 2017). Interestingly, an effect on fracture toughness was not detectable and all the mAESO-based nanocomposites were brittle, having fracture toughness values of approximately 0.8 MPa$\sqrt{m}$.

The sustainable bio-derived IM and mAESO resin-based nanocomposites studied in this work have better tensile mechanical properties than other polymer nanocomposites

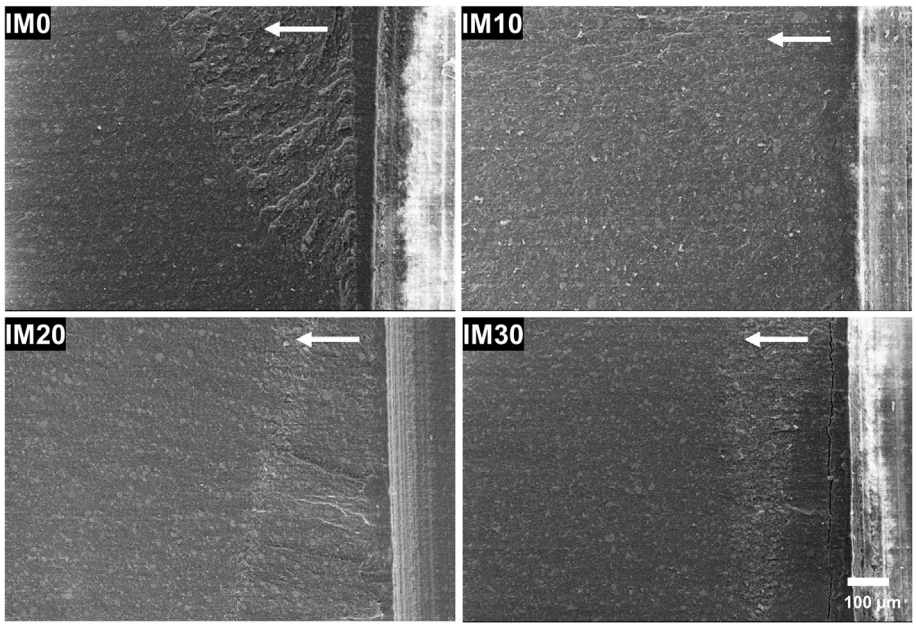

FIGURE 7 | SEM images of the fracture surfaces of the nanocomposite beams after Mode-I plane strain fracture testing.

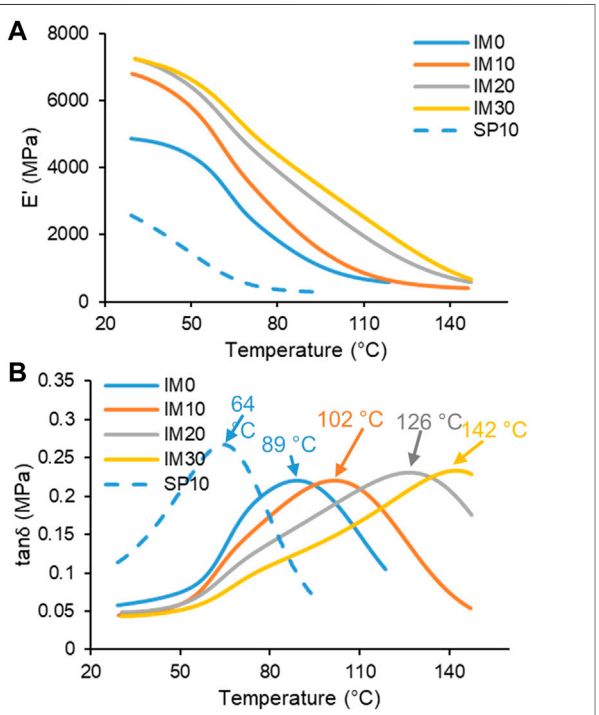

FIGURE 8 | Data from dynamic mechanical analysis of the 3D printed nanocomposites. **(A)** storage modulus (E′), and **(B)** damping coefficient (tanδ) as functions of temperature. The T_g values were determined from the peaks of the tanδ vs temperature plots. The dotted blue line belongs to SP10, an AESO/PEGDA/nHA based nanocomposite from our previous work (Mondal et al., 2021), analogous to IM0.

reported in the literature that used polymers from petroleum or natural origin composited with nHA. For instance, nanocomposites made of 20 wt% nHA and poly (methylmethacrylate) (PMMA) had tensile fracture strength of 39.3 MPa (Yang et al., 2013). Epoxy resin with 10 wt% nHA had tensile fracture strength of 35–45 MPa and Young's modulus of 1.5–2.0 GPa (Jaramillo et al., 2020). Nanocomposites of poly (butylene succinate-co-ethylene terephthalate) and 10 wt % nHA had tensile fracture strength of 29.8 MPa (Shirali et al., 2016). Nanocomposites of 3,4-dihydroxycinnamic acid (DHCA), 10-hydroxydecanoic acid (HDA), and nHA (20 wt%) had tensile fracture strength of 5–9 MPa (Dong et al., 2013). The tensile fracture strength and modulus of our previous 3D printed nanocomposite SP10 were 30 MPa and 2 GPa, respectively (Mondal et al., 2021). In this work, the tensile fracture strength and modulus of IM30 were found to be 67.9 ± 7.4 MPa and 7.9 ± 3.6 GPa, respectively.

The strain-at-fracture or the ductility of the nanocomposites can be improved by increasing the content of mAESO, but it will decrease the stiffness of the nanocomposites. Another effective way to improve the strength of polymer nanocomposites is to improve the dispersion of the nanoparticles in the polymer matrices. In this work, the SEM images of the polished 3D printed nanocomposite surfaces revealed the presence of agglomerates of up to ~10 µm in diameter. These may act as stress concentrations, limiting the tensile strength and fracture toughness of the nanocomposites. Future work must strive to achieve improved nanoparticle dispersion and ideally greater strength.

DMA was performed to understand the effect of replacing PEGDA with IM on the glass transition temperature of the 3D printed nanocomposites. Both the storage modulus and T_g increased due to the replacement of AESO with mAESO and PEGDA with IM. Replacing AESO with mAESO effectively increased the crosslinking in the matrix as evidenced by the greater tensile strength of mAESO-based nanocomposites. The increased degree of crosslinking in mAESO and IM containing nanocomposites also increased T_g. T_g of the 3D-printed IM30 nanocomposite is 142°C, whereas the T_g of the SP10 was 64°C and IM0 was 89°C.

CONCLUSION

This paper demonstrates novel mSLA-based 3D printing of highly sustainable mAESO/nHA/PEGDA/IM nanocomposites, and their excellent tensile, fracture, and dynamic mechanical properties. Switching from AESO to mAESO greatly decreased ink viscosity and improved printability, and improved the mechanical properties of the printed nanocomposite material. Partially replacing PEGDA, a petroleum-based oligomer, with bio-based IM as the reactive diluent in the resin improved the sustainability profile of the material and greatly improved the tensile fracture strength and Young's modulus. However, these nanocomposites are glassy and brittle at room temperature due to being well below their glass transition temperature. Future work towards greater mechanical performance must address nanoparticle dispersion and the brittleness of the resulting nanocomposites.

DATA AVAILABILITY STATEMENT

The raw data supporting the conclusion of this article will be made available by the authors, without undue reservation.

AUTHOR CONTRIBUTIONS

DM is the lead author having conducting a great deal of the experiments and data analysis. He synthesized the functionalized biopolymer components of the nanocomposites and he wrote the first draft of the paper. ED assisted with methodologies, conducting the experiments and data analysis. Furthermore, she edited and revised the manuscript. TW is the PI of the lab where this work was conducted. He supervised the work of his two co-authors, collaborated regarding concept generation, methodologies, testing and analysis, acquired the funding, and he extensively edited and revised the manuscript.

FUNDING

This work was supported by the Natural Sciences and Engineering Research Council of Canada, the Canadian Institutes of Health Research, the Canada Foundation for Innovation, the Ontario Research Fund, and the University of Waterloo's Dean of Engineering.

ACKNOWLEDGMENTS

The authors thank Teresa Diamante Marotta for her assistance with mechanical testing.

SUPPLEMENTARY MATERIAL

The Supplementary Material for this article can be found online at: https://www.frontiersin.org/articles/10.3389/fmats.2022.833065/full#supplementary-material

REFERENCES

Amulya, K., Katakojwala, R., Ramakrishna, S., and Venkata Mohan, S. (2021). Low Carbon Biodegradable Polymer Matrices for Sustainable Future. *Composites C: Open Access* 4, 100111. doi:10.1016/j.jcomc.2021.100111

ASTM (2016). *Standard Test Methods for Plane-Strain Fracture Toughness and Strain Energy Release Rate of Plastic Materials*. West Conshohocken: ASTM. doi:10.1520/D5045-14

ASTMD3039 (2017). *Standard Test Method for Tensile Properties of Polymer Matrix Composite Materials*. West Conshohocken: ASTM. doi:10.1520/D3039_D3039M-17

Babu, R. P., O'Connor, K., and Seeram, R. (2013). Current Progress on Bio-Based Polymers and Their Future Trends. *Prog. Biomater.* 2, 8. doi:10.1186/2194-0517-2-8

Bertomeu, D., García-Sanoguera, D., Fenollar, O., Boronat, T., and Balart, R. (2012). Use of Eco-Friendly Epoxy Resins from Renewable Resources as Potential Substitutes of Petrochemical Epoxy Resins for Ambient Cured Composites with Flax Reinforcements. *Polym. Compos.* 33, 683–692. doi:10.1002/pc.22192

Campanella, A., La Scala, J. J., and Wool, R. P. (2009). The Use of Acrylated Fatty Acid Methyl Esters as Styrene Replacements in Triglyceride-Based Thermosetting Polymers. *Polym. Eng. Sci.* 49, 2384–2392. doi:10.1002/pen.21486

Campanella, A., Scala, J. J. L., and Wool, R. P. (2011). Fatty Acid-Based Comonomers as Styrene Replacements in Soybean and castor Oil-Based Thermosetting Polymers. *J. Appl. Polym. Sci.* 119, 1000–1010. doi:10.1002/app.32810

Comeau, P., and Willett, T. (2018). Impact of Side Chain Polarity on Non-stoichiometric Nano-Hydroxyapatite Surface Functionalization with Amino Acids. *Sci. Rep.* 8, 12700. doi:10.1038/s41598-018-31058-5

de Bruijn, J. D., Klein, C. P. A. T., de Groot, K., and van Blitterswijk, C. A. (1992). The Ultrastructure of the Bone-Hydroxyapatite Interfacein Vitro. *J. Biomed. Mater. Res.* 26, 1365–1382. doi:10.1002/jbm.820261008

Dong, W., Ren, J., Shi, D., Ma, P., Li, X., Duan, F., et al. (2013). Hydrolyzable and Bio-Based Polyester/nano-Hydroxyapatite Nanocomposites: Structure and Properties. *Polym. Degrad. Stab.* 98, 1790–1795. doi:10.1016/j.polymdegradstab.2013.05.015

Fenouillot, F., Rousseau, A., Colomines, G., Saint-Loup, R., and Pascault, J.-P. (2010). Polymers from Renewable 1,4:3,6-dianhydrohexitols (Isosorbide, Isomannide and Isoidide): A Review. *Prog. Polym. Sci.* 35, 578–622. doi:10.1016/j.progpolymsci.2009.10.001

Galbis, J. A., García-Martín, M. d. G., de Paz, M. V., and Galbis, E. (2016). Synthetic Polymers from Sugar-Based Monomers. *Chem. Rev.* 116, 1600–1636. doi:10.1021/acs.chemrev.5b00242

Gonzalez, G., Chiappone, A., Roppolo, I., Fantino, E., Bertana, V., Perrucci, F., et al. (2017). Development of 3D Printable Formulations Containing CNT with Enhanced Electrical Properties. *Polymer* 109, 246–253. doi:10.1016/j.polymer.2016.12.051

Han, D., Yang, C., Fang, N. X., and Lee, H. (2019). Rapid Multi-Material 3D Printing with Projection Micro-stereolithography Using Dynamic Fluidic

Control. *Additive Manufacturing* 27, 606–615. doi:10.1016/j.addma.2019.03.031

Jaramillo, A. F., Medina, C., Flores, P., Canales, C., Maldonado, C., Castaño Rivera, P., et al. (2020). Improvement of Thermomechanical Properties of Composite Based on Hydroxyapatite Functionalized with Alkylsilanes in Epoxy Matrix. *Ceramics Int.* 46, 8368–8378. doi:10.1016/j.ceramint.2019.12.069

La Scala, J., and Wool, R. P. (2005). Property Analysis of Triglyceride-Based Thermosets. *Polymer* 46, 61–69. doi:10.1016/j.polymer.2004.11.002

Ligon, S. C., Liska, R., Stampfl, J., Gurr, M., and Mülhaupt, R. (2017). Polymers for 3D Printing and Customized Additive Manufacturing. *Chem. Rev.* 117, 10212–10290. doi:10.1021/acs.chemrev.7b00074

Liu, W., Xie, T., and Qiu, R. (2017). Biobased Thermosets Prepared from Rigid Isosorbide and Flexible Soybean Oil Derivatives. *ACS Sustain. Chem. Eng.* 5, 774–783. doi:10.1021/acssuschemeng.6b02117

Llevot, A. (2017). Sustainable Synthetic Approaches for the Preparation of Plant Oil-Based Thermosets. *J. Am. Oil Chem. Soc.* 94, 169–186. doi:10.1007/s11746-016-2932-4

Mauck, S. C., Wang, S., Ding, W., Rohde, B. J., Fortune, C. K., Yang, G., et al. (2016). Biorenewable Tough Blends of Polylactide and Acrylated Epoxidized Soybean Oil Compatibilized by a Polylactide Star Polymer. *Macromolecules* 49, 1605–1615. doi:10.1021/acs.macromol.5b02613

Mondal, D., Haghpanah, Z., Huxman, C. J., Tanter, S., Sun, D., Gorbet, M., et al. (2021). mSLA-based 3D Printing of Acrylated Epoxidized Soybean Oil - Nano-Hydroxyapatite Composites for Bone Repair. *Mater. Sci. Eng. C* 130, 112456. doi:10.1016/j.msec.2021.112456

Mondal, D., and Willett, T. L. (2020). Mechanical Properties of Nanocomposite Biomaterials Improved by Extrusion during Direct Ink Writing. *J. Mech. Behav. Biomed. Mater.* 104, 103653. doi:10.1016/j.jmbbm.2020.103653

Moon, B.-U., Tsai, S. S. H., and Hwang, D. K. (2015). Rotary Polymer Micromachines: *In Situ* Fabrication of Microgear Components in Microchannels. *Microfluid Nanofluid* 19, 67–74. doi:10.1007/s10404-015-1548-6

Mu, Q., Wang, L., Dunn, C. K., Kuang, X., Duan, F., Zhang, Z., et al. (2017). Digital Light Processing 3D Printing of Conductive Complex Structures. *Additive Manufacturing* 18, 74–83. doi:10.1016/j.addma.2017.08.011

Muenks, D., and Kyosev, Y. (2021). Productivity Comparison between Vat Polymerization and Fused Filament Fabrication Methods for Additive Manufacturing of Polymers. *3D Printing and Additive Manufacturing*. doi:10.1089/3dp.2021.0009

Pelletier, H., and Gandini, A. (2006). Preparation of Acrylated and Urethanated Triacylglycerols. *Eur. J. Lipid Sci. Technol.* 108, 411–420. doi:10.1002/ejlt.200501168

Podgórski, M., Huang, S., and Bowman, C. N. (2021). Additive Manufacture of Dynamic Thiol-Ene Networks Incorporating Anhydride-Derived Reversible Thioester Links. *ACS Appl. Mater. Inter.* 13, 12789–12796. doi:10.1021/acsami.0c18979

Rosa, A. L., Beloti, M. M., Oliveira, P. T., and Van Noort, R. (2002). Osseointegration and Osseoconductivity of Hydroxyapatite of Different Microporosities. *J. Mater. Sci. Mater. Med.* 13, 1071–1075. doi:10.1023/A:1020305008042

Sadler, J. M., Nguyen, A.-P. T., Toulan, F. R., Szabo, J. P., Palmese, G. R., Scheck, C., et al. (2013). Isosorbide-methacrylate as a Bio-Based Low Viscosity Resin for High Performance Thermosetting Applications. *J. Mater. Chem. A.* 1, 12579–12586. doi:10.1039/C3TA12918G

Saxon, D. J., Luke, A. M., Sajjad, H., Tolman, W. B., and Reineke, T. M. (2020). Next-generation Polymers: Isosorbide as a Renewable Alternative. *Prog. Polym. Sci.* 101, 101196. doi:10.1016/j.progpolymsci.2019.101196

Schneiderman, D. K., and Hillmyer, M. A. (2017). 50th Anniversary Perspective: There Is a Great Future in Sustainable Polymers. *Macromolecules* 50, 3733–3749. doi:10.1021/acs.macromol.7b00293

Shirali, H., Rafizadeh, M., and Taromi, F. A. (2016). *In Situ* polymerized Poly(butylene Succinate-Co-Ethylene Terephthalate)/hydroxyapatite Nanocomposite with Adjusted thermal, Mechanical and Hydrolytic Degradation Properties. *Macromol. Res.* 24, 900–908. doi:10.1007/s13233-016-4131-4

Song, B., Chen, W., Liu, Z., and Erhan, S. (2006). Compressive Properties of Epoxidized Soybean Oil/clay Nanocomposites. *Int. J. Plasticity* 22, 1549–1568. doi:10.1016/j.ijplas.2005.10.004

Stansbury, J. W., and Idacavage, M. J. (2016). 3D Printing with Polymers: Challenges Among Expanding Options and Opportunities. *Dental Mater.* 32, 54–64. doi:10.1016/j.dental.2015.09.018

Wang, B.-T., Lu, F.-D., Xu, F., Li, Y.-Z., and Kessler, M. R. (2016). Synthesis of Renewable Isosorbide-Based Monomer and Preparation of the Corresponding Thermosets. *Chin. Chem. Lett.* 27, 875–878. doi:10.1016/j.cclet.2016.01.030

Webster, T., Ergun, C., Doremus, R. H., Siegel, R. W., and Bizios, R. (2000). Enhanced Functions of Osteoblasts on Nanophase Ceramics. *Biomaterials* 21, 1803–1810. doi:10.1016/S0142-9612(00)00075-2

Wilbon, P. A., Swartz, J. L., Meltzer, N. R., Brutman, J. P., Hillmyer, M. A., and Wissinger, J. E. (2017). Degradable Thermosets Derived from an Isosorbide/Succinic Anhydride Monomer and Glycerol. *ACS Sustain. Chem. Eng.* 5, 9185–9190. doi:10.1021/acssuschemeng.7b02096

Yang, B., Li, M., Wu, Y., Huang, J., Zhang, H., and Deng, C. (2012). Preparation and Characterization of Bone-like Hydroxyapatite/poly(methyl Methacrylate) Composite Biomaterials. *Sci. Eng. Compos. Mater.* 20, 1–7. doi:10.1515/secm-2012-0079

Zhu, Y., Romain, C., and Williams, C. K. (2016). Sustainable Polymers from Renewable Resources. *Nature* 540, 354–362. doi:10.1038/nature21001

Conflict of Interest: The authors declare that the research was conducted in the absence of any commercial or financial relationships that could be construed as a potential conflict of interest.

Publisher's Note: All claims expressed in this article are solely those of the authors and do not necessarily represent those of their affiliated organizations, or those of the publisher, the editors and the reviewers. Any product that may be evaluated in this article, or claim that may be made by its manufacturer, is not guaranteed or endorsed by the publisher.